Effect of edge magnetic island on carbon screening in the J-TEXT tokamak

X.L. Zhang (张晓龙)[1,2], Z.F. Cheng (程芝峰)[3]a), S. Zhou (周松)[3], Y Liang (梁云峰) [3,4], W. Yan (严伟) [3], N.C. Wang (王能超) [3], X.Y. Zhang (张霄翼) [3], Z.H. Jiang (江中和) [3], Z.J. Yang (扬州军) [3], X. Xu (徐鑫) [3], D. Li (李达)[3], Q. Li (李琼) [3], X.D. Lin (林晓东)[1,2], Y.H. Ding (丁永华) [3], Z.Y. Chen (陈忠勇) [3], Z.P. Chen (陈志鹏) [3] and J-TEXT Team[3,b]

[1] *Advanced Energy Research Center, Shenzhen University, Shenzhen 518060, China*

[2.] *Key Laboratory of Optoelectronic Devices and Systems of Ministry of Education and Guangdong Province, College of Optoelectronic Engineering, Shenzhen University, Shenzhen 518060,China*

[3] *State Key Laboratory of Advanced Electromagnetic Engineering and Technology, School of Electrical and Electronic Engineering, Huazhong University of Science and Technology, Wuhan 430074, China*

[4] *Forschungszentrum Jülich GmbH, Institut für Energieund Klimaforschung-Plasmaphysik, 52425 Jülich, Germany*

[a] *chengfe@hust.edu.cn*

[b] *See the author list of "Y. Liang et al 2019 Overview of the Recent Experimental Research on the J-TEXT Tokamak, Nucl. Fusion 59 112016"*

Abstract

The effect of externally applied resonant magnetic perturbation (RMP) on carbon impurity behavior is investigated in the J-TEXT tokamak. It's found that the m/n = 3/1 islands has the impurity screening effect, which becomes obvious while the edge magnetic island is generated via the RMP field penetration. The impurity screening effect shows a dependence on the RMP phase with the field penetration, to be strongest if the O point of the magnetic island is near the low-field-side (LFS) limiter plate. By combining the methane injection experimental study and the STRAHL impurity transport analysis, we found that the variation of the impurity transport dominates the impurity screening effect. The impurity diffusion at the inner plasma region ($r/a < 0.8$) is enhanced with a significant increase of outward convection velocity at the edge region in the case of the magnetic island's O point near the LFS limiter plate. The impurity transport coefficient varies in much less level for the case with magnetic island's X point near the LFS limiter plate. The interaction of the magnetic island and the LFS limiter plate is thought to contribute to the impurity transport variation, with the dependence on the RMP phase. The possible reason is that the interaction between the magnetic island and the LFS limiter.

Keywords: magnetic island, impurity transport, RMP, boundary plasma physics, J-TEXT tokamak

(Some figures may appear in color only in the online journal)

I. INTRODUCTION

Impurities affect plasma equilibrium, degrade plasma confinement, and even excite MHD instability, leading to plasma disruption by increasing plasma radiation loss and resistivity. Thus, it is taken great efforts to reduce plasma impurity concentration on most magnetic confinement devices. Effectively controlling impurity is particularly critical for the International Thermonuclear Experimental Reactor (ITER) to achieve the desired fusion gain goal, with the insufficient heating power [1].

The magnetic field geometry is considered to play an important role in plasma particle control due to the strong anisotropy of particle transport respected to magnetic field vectors. Thus, the possibility of controlling the edge plasma behavior by changing the edge magnetic field structure has been studied in several devices, e.g., LHD [2,3], TEXTOR-DED [4,5] DIII-D [6]. In these cases, the external magnetic coils, named Resonant Magnetic Perturbation (RMP) or Dynamic Ergodic Divertor (DED) coils, are used to offer the RMP, which leads to near-field effects forming chains of magnetic islands. The magnetic island chains may overlap, resulting in a strong modification of the original magnetic structure [7].

In TEXTOR DED operation, they found a so-called Pump Out effect, which is also observed in DIII-D [8], EAST [9], and JET [10] during ELM mitigation experiments with RMP, characterized by a decrease in the plasma density. Pump Out effect appears in the J-TEXT RMP experiments with m/n=2/1 field penetration [11]. However, under the m/n=3/1 RMP, the electron density is found to increase in some scenarios due to the enhanced edge recycling [12].

Under the same regime, impurity behavior has been found effectively affected by RMP on various devices either [13-15]. It is widely reported that the impurity concentration is reduced with the introduction of RMP in both L- and H- mode plasma. Carbon de-contaminations in the core plasma are observed under various RMP modes in TEXTOR [16] and LHD [17]. Fluorine concentration is found to be reduced in DIII-D ELM suppression experiment by RMP [18]. Furthermore, RMP is reported to reduce the concentration of higher charge impurities, such as argon/iron in TEXTOR [19], and tungsten/iron in EAST [20].

The role of RMP in reducing the impurity concentration is explored from the perspectives of the impurity transport and impurity source. In the TEXTOR DED experiment with the basic mode of m/n=3/1, a reduction in carbon confinement time proportional to I_{DED} agrees with a diffusion-dominated analytical model, where the I_{DED} is the coil current [16]. Changes in the effective radial transport caused by classical parallel diffusivity along the stochastic field lines are believed to account for the changes in particle (and impurity) transport [21]. The RMP-induced magnetic island may modify the electron or ion flow towards the wall, resulting in a change of the radial electric field [19]. The possible mechanisms of the RMP effect on impurity transport are also reported in [22-24]. In DIII-D, the STRAHL code is applied to simulate the fluorine emissivity evolution in the RMP ELM suppressed plasma [16]. The impurity convection is found to become slightly positive due to the strong ion temperature gradient, which acts to screen impurities. The larger diffusion coefficient D~5-10 m^2/s is also favorable for reducing impurity concentration. In EAST H-mode plasmas, the RMPs increase the diffusion coefficient and the outward convective velocity through the STRAHL simulation for iron spectra (Fe^{20+} 12.88nm, Fe^{21+} 11.63nm, Fe^{22+} 13.29nm) [13].

Since the outward flux is significantly modified by RMP, it also affects the plasma-wall interaction (PWI) and the production of impurity at the boundary. Strong local recycling is generally observed with the enhanced outward flux in DIII-D [25, 26], J-TEXT [12], MST [27] etc. The experimental results on DIII-D show that gross erosion differs significantly (>50%) at the different toroidal phases of the RMP field, consistent with a substantially three-dimensional (3D) impact [28].

The RMP coils on the J-TEXT could work at various RMP modes providing flexible experimental conditions to explore the RMP effect on the impurity transport. This paper specifically investigated the edge magnetic island topology's impact on the carbon source (Limiter) and the impurity transport correspondingly. The structure of the paper is as blow. In section 2, the experimental setups are given, and then the experimental results are described in section 3. In section 4, the carbon transport coefficients are analyzed with STRAHL code, and the effect of 3/1 magnetic island on LFS limiter is discussed. It is summed up in section 5.

II. Experimental Setup

J-TEXT (formerly TEXT-U) is a conventional tokamak with silicon carbide graphite limiter [29, 30, 31]. It has the major radius of 1.05m, and the minor radius of 0.25m~0.27m. The typical discharge parameters are as follows: plasma current 100~220 kA, toroidal field 1.4T~2.2T, the line averaged electron density $1\sim6\times10^{19}/m^3$. There are two sets of resonant magnetic perturbation coils constructed on the J-TEXT tokamak, which are placed around the torus uniformly [32, 33, 34]. As shown in FIG. 1(a), the RMP system consists of 24 saddle coils divided into two groups colored in blue and red, respectively. FIG. 1 (b) shows the spectrum of the RMP field when the 3/1 RMP component is dominant. The parameter ϕ_o is defined to characterize the phase of the 3/1 magnetic island under the vacuum assumption. It refers to the toroidal angle of the O point for the 3/1 magnetic island with the poloidal angle at $\theta = 0$ degrees, i.e. in the low field side (LFS) mid-plane. The phase of $\phi_o=0$ is as marked in FIG. 1 (a). The RMP amplitude and the spatial phase can be adjusted by changing the coil current and configuration. In the study, various 3/1 RMP configurations are applied to investigate the impurity behaviors.

With the graphite limiter and the graphite tiles fully covering the vacuum wall at the high field side, it is foreseen that abundant carbon impurities exist in the J-TEXT plasma. Since the typical electron temperature is about 800-1000 eV in the core and 10-50 eV near the LCFS (Last Closed Flux Surface) in the J-TEXT plasma, the carbon ions can distribute across a relatively wide radial range in the plasma, making them a good candidate for the impurity study. We have developed a spectral diagnostic system to observe carbon ions. It consists of carbon V (C V 227.09 nm), carbon III (C III 464.7 nm), and carbon VI (C VI 529.26 nm) diagnostics [35], as shown in FIG.2. Two identical 18-channel photodiode arrays (PDAs) with the specified front C III filter (center wavelength of 466 nm, bandwidth of 5 nm) at port 4 are dedicated to measuring the C III emission in the high-field side (HFS) and low-field side (LFS). The spatial resolution, time resolution, and coverage area of C III diagnostic are 13 mm, 100 μs, and r = 7 cm~ 29 cm, respectively. The C V and C VI diagnostic are developed to measure the inner carbon emission profile. The high-resolution spectroscopy system consists of a 1.33-m-focal-length monochromator, an ANDOR EMCCD camera with 1024 × 1024 pixels and each size of 13 μm × 13 μm, and a fiber optic light collection system with 16 viewing channels. It is adjusted to

measure the spectra of C III (229.69 nm) and C V (227.09 nm) at the LFS, which could provide the carbon emission intensity and rotation as required.

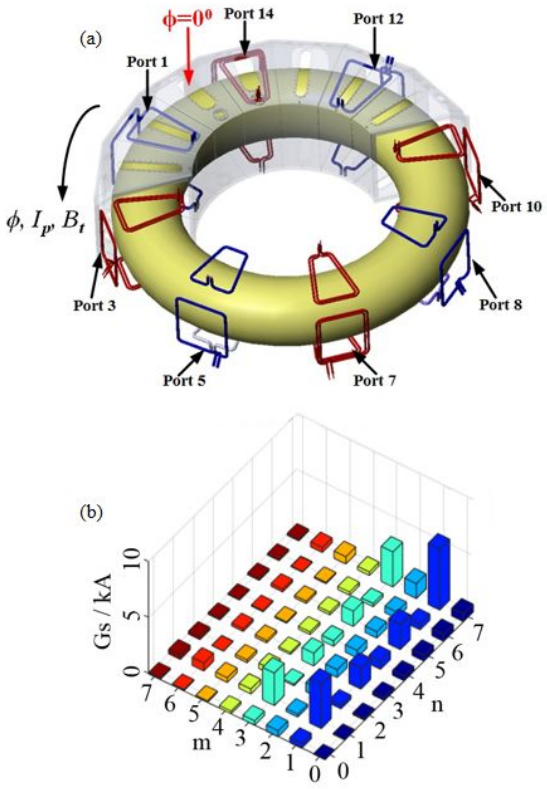

FIG. 1. (a) Layout of the RMP coils on the J-TEXT tokamak; (b) Spectrum of the perturbation field when 3/1RMP dominant.

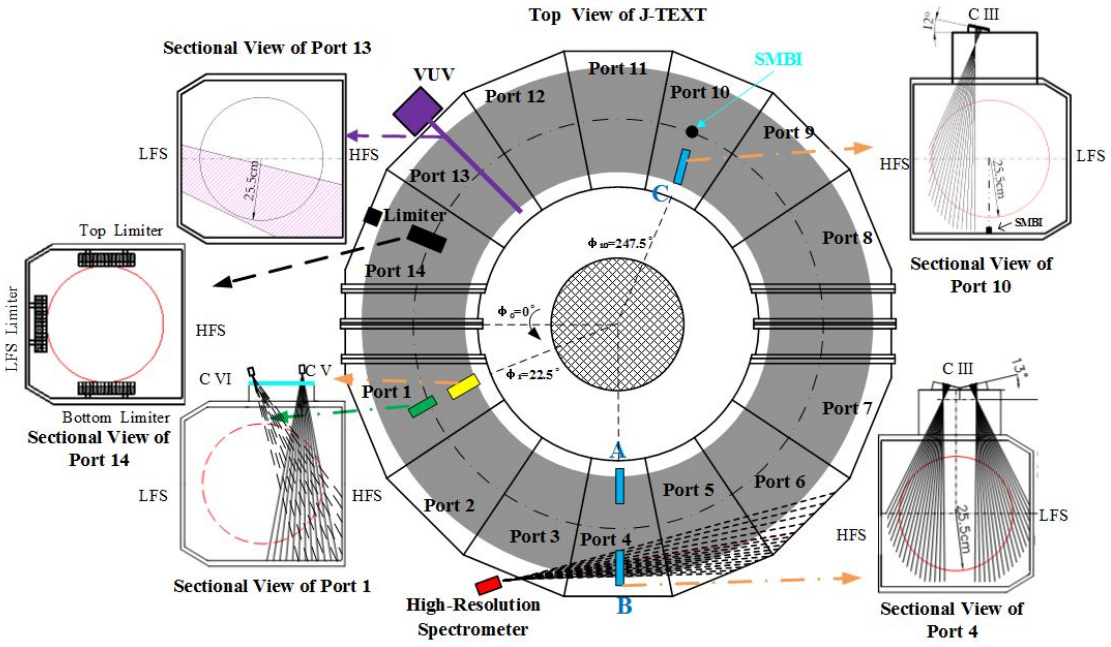

FIG. 2. Layout and composition of the spectral diagnostic system on the J-TEXT tokamak. The yellow block and green block denote the carbon V diagnostic and the carbon VI diagnostic in the HFS of Port 1, respectively; the three blue blocks (A, B, C) denote the carbon III diagnostics in the HFS of Port 4, LFS of Port 4, and HFS of Port 10, respectively; the red block denotes the

high-resolution spectrometer in the horizontal plane of Port 3; the purple block denotes the vacuum ultraviolet (VUV) spectroscopy diagnostic; the black blocks in the left figure represent the three limiters layout; the black point in port 10 represent the position of SMBI nozzle.

A space-resolved Vacuum Ultraviolet (VUV) spectroscopy system based on a 1-meter normal incidence spectrometer has been developed on the J-TEXT tokamak [36, 37], to observe the highly ionized impurity closer to the plasma center. In this experiment, the VUV diagnostic is set to observe the Si XII (49.9nm).

The electron density profile comes from laser-based Polarimeter-Interferometer system (POLARIS) [38, 39]; the electron temperature profile comes from the Electron Cyclotron Emission (ECE) [40]; the ion temperature comes from an X-ray imaging crystal spectroscopy system (XICS) [41] for Ar^{16+} in the core and high-resolution spectroscopy diagnostic [42, 43] for C^{2+} or C^{4+} near the edge. Furthermore, a Supersonic Molecular Beam Injection (SMBI) System is applied to inject impurity gas in this experiment [44, 45]. The injector is equipped at the bottom of port 10 with the pre-filled gas pressure of 1.0 MPa, which can inject 0.8×10^{19} particles through a 0.5ms pulse in this experiment.

III. Experimental Results

3.1 Impurity behavior under 3/1 RMP

In order to understand the edge impurity behavior under the 3/1 RMP, the line emission signals from multiple ionized carbon and Si XII are collected for comparison under various RMP parameters. Taking the typical discharge 1053337 as an example (plasma parameters: I_p = 170 kA, B_T = 1.75 T, q_a ~ 3.2), we can find that a 3/1 locked magnetic island is induced due to the 3/1 RMP penetration when the current intensity exceeds a certain value (~ 3kA), as shown in FIG. 3. In this case, a rapid change of toroidal impurity rotation is found, where a typical rise of ~ 5-8 km/s in the co-current direction for the C V (or C VI) rotation appears. A slight decrease (< 5%) in center electron density and edge electron density characterized by POLARIS. But no significant variation is observed in the electron temperature characterized by ECE.

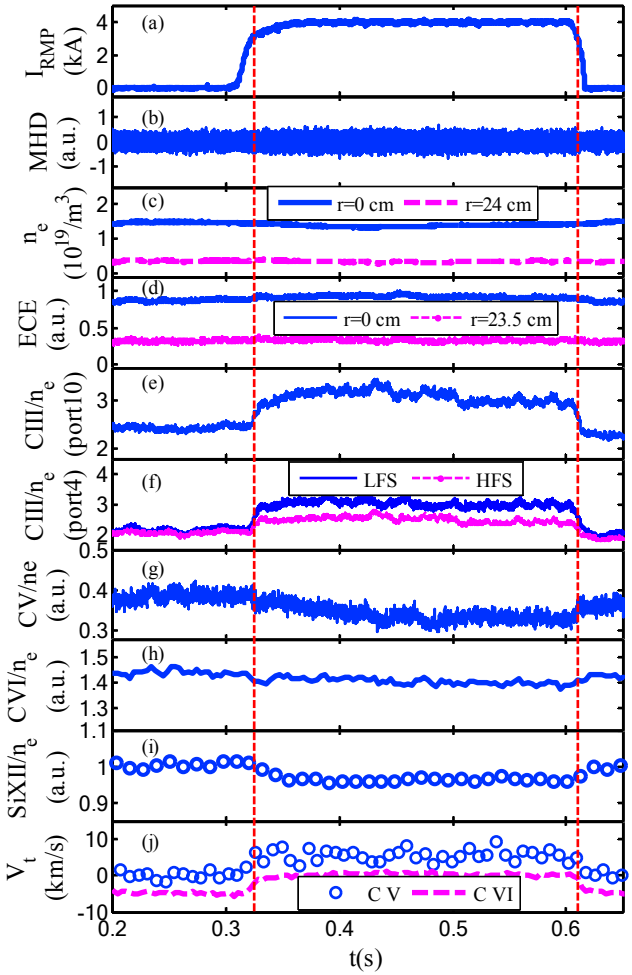

FIG. 3. Evolution of plasma parameters at shot 1053337. (a) RMP current, (b) Mirnov coil signal, (c) line-averaged density at r= 0 cm (blue) and r=24 cm (pink), (d) central and edge ECE signal (e) carbon III signal (r=24 cm) at HFS of port 10 (as shown in FIG. 2 blue area C), (f) C III signal at HFS (r= 24 cm, pink) and LFS (r= 24 cm, blue) of port 4 (as shown in FIG. 2 blue area A and B), (g) ratio of C V to electron density (r= 20 cm) at HFS of port 1 (as shown in FIG. 2 yellow area), (h) ratio of C VI to electron density (r=15cm) at HFS of port 1 (as shown in FIG. 2 green area), (i) ratio of silicon XII to electron density measured by VUV diagnostic, (j) toroidal rotation velocity of C V and C VI. The red dotted lines indicate 3/1 penetration begin and end.

All impurity line emission signals are presented with the ratio to the local density to eliminate the signal deviation from density variation, which provide more reasonable evaluation of the impurity concentration. In FIG. 3, the C III intensity near the plasma boundary (FIG. 3 (e) and (f)) increases by 30-50% while the RMP penetration happens at 0.325 s. This means that the carbon accumulates near the LCFS. The C III signal is commonly believed to represent the amount of carbon source at the plasma edge. It is also found that the variations of C III signals at different toroidal and poloidal positions are not the same (port 10 CIII: 30%, port 4 LFS CIII: 50%, port 4 HFS CIII: 35%) , which is thought to be caused by the three-dimensional effect of the 3/1 magnetic island at the edge region. The role of 3/1 magnetic island on C V (at r~20 cm) and C VI (at r~15 cm) emission is relatively weak. After the formation of 3/1 locked magnetic island, the C V intensity has a slight decrease (~ 10%); for C VI, the intensity decrease ~ 5%. The Si XII

emission measured by VUV diagnosis also decreases a bit (~ 5%) after the formation of 3/1 locked island. This means that all the observed impurity contents at the inner place reduce, concluding that the edge magnetic island may benefit the impurity exhaust. It may be attributed to the impurity screening effect [16, 19, 46].

The emission intensity ratio of the inner impurity (C V or C VI) and the outer impurity (C III) is used to reflect the carbon screening effect, as shown in FIG. 4. Since the three-dimensional edge magnetic topology leads to an asymmetric C III distribution, the C III signal is deduced by averaging the C III signals from multiple places. It is found that the impurity screening effect increases with the increase of RMP current, showing the decline of the ratio of $I_{C\ V}$ / $I_{C\ III}$. The effect appears much sensitive on the RMP penetration, with $I_{RMP} \geq 3.2$ kA, corresponding to the further significant drop after the red dash line in FIG. 4 (b). The RMP phase is found to impact the impurity screening effect either, showing that the normalized ratio of $I_{C\ V}$ / $I_{C\ III}$ in the case with ϕ_o= 134° RMP penetration is higher than that with ϕ_o= 66°.

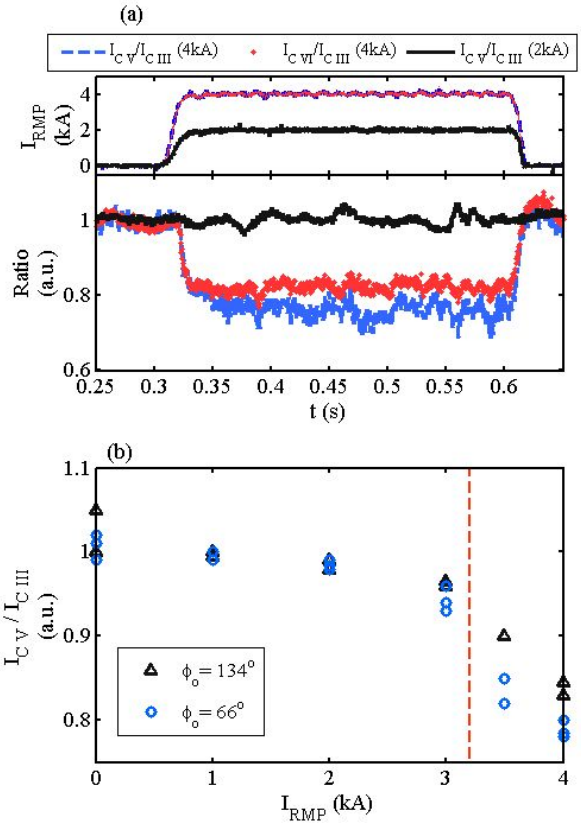

FIG. 4. (a) Current of RMP, the evolution of the ratio of $I_{C\ V}$/ $I_{C\ III}$ (blue dotted line) and $I_{C\ VI}$/ $I_{C\ III}$ (red dot) with I_{RMP}= 4kA, $I_{C\ V}$/ $I_{C\ III}$ (black line) with I_{RMP}= 2kA; (b) Statistical relationship between ratio of $I_{C\ V}$/ $I_{C\ III}$ I and RMP current, Red dash means the threshold of 3/1 penetration.

3.2 The effect of different phase on impurity behavior

With the localized limiters in the J-TEXT vacuum vessel, a quick assumption is that the three-dimensional plasma configuration caused by the edge magnetic field will lead to the various interaction with the vacuum material (limiter material) under different RMP phases. Thus, the impurity source may be coupled with the RMP phase. To explore the detailed impacts, we compared the carbon impurity behaviors under four different RMP phases with ϕ_o = -24°, 156°,

-54° and 126°, respectively. The detailed RMP configurations are presented in Table 1. The LFS limiter is located at the mid-plane of port 14 (as shown in FIG. 2), and the corresponding toroidal angle is -22.5°. It can be seen that the O point of the magnetic island is closest to the LFS limiter (referred to as *the O point case*) under the phases ϕ_o = -24°; the X point is closest to the LFS limiter at ϕ_o = 156° (referred to as *the X point case*).

Table 1. RMP Phases configuration

Shot	1056677	1058410	1058407	1056693
Phase of island (ϕ_o)	-24°	-54°	126°	156°
Remark	O point case			X point case

The evolutions of C V and C III signals in the four RMP phases are presented in FIG. 5, where the RMP fields are added at the same time as that in FIG. 3. It shows that the intensity of C III in O point case (ϕ_o = -24°) and X point case (ϕ_o = 156°) increases ~40% and ~20%, respectively. The variation of C III intensity at ϕ_o = -54° and 126° are at the intermediate values. However, the evolution of the C V signal is in the opposite trend. C V emission at phase ϕ_o = 156° almost keeps constant, but drops in the most at ϕ_o = -24°, indicating the strongest impurity screening effect among the four cases.

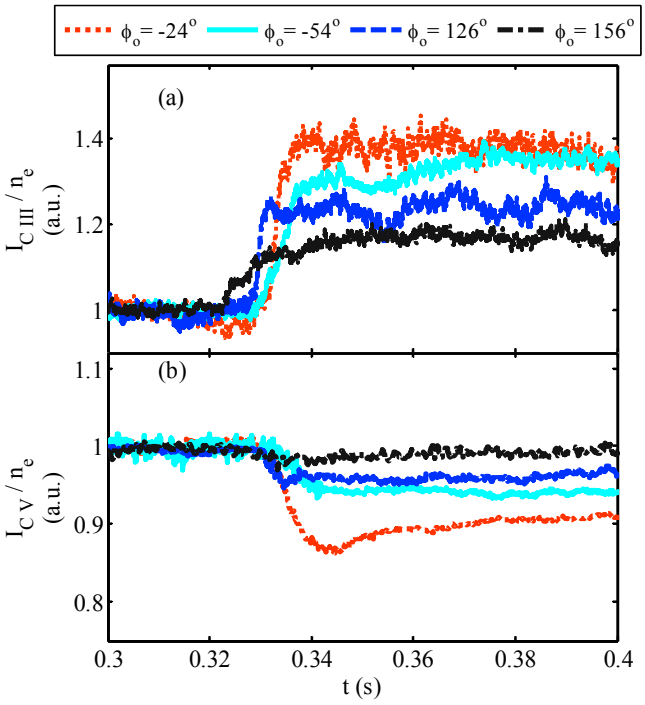

FIG. 5. The different island phase effects on impurity line emission. (a) I_{CV}/n_e; (b) $I_{C\ III}/n_e$ (ϕ_o = -24°: red dot, ϕ_o = -54°: cyan line, ϕ_o = 126°: blue dash, ϕ_o = 156°: black dash-dot)

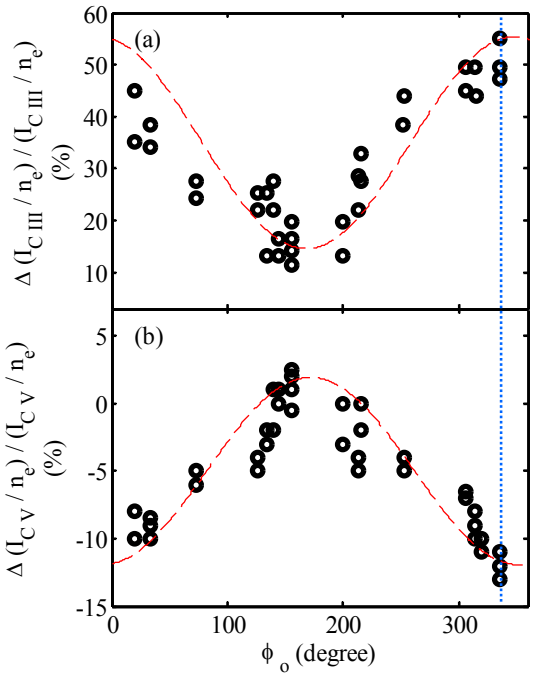

FIG. 6. Normalized statistical results of RMP phase (ϕ_o) and relative variation of the $I_{C\ V}/n_e$ and $I_{C\ III}/n_e$ with 3/1 locked magnetic island induced by the RMP penetration. The blue dotted line indicates the LFS limiter position.

By modifying the RMP coil connection configuration, we could obtain multiple 3/1 RMP phases. FIG. 6 presents the relative variation of C V and C III emission with the scanned RMP phases, where the plasma parameters are fixed as I_P = 170 kA, B_T = 1.7 T, n_e = 1.2 ~ 1.5 × 10^{19} / m^3. The field penetrations are induced by using the same RMP strength with the coil current of 4 kA. The dependence of the carbon emission on RMP phase can be well described by $\Delta I/n_e = b + k * \sin(\phi_o + \alpha)$ for both C V and C III, where k, a and b are constant. However, the ϕ_o dependence is opposite for the two impurity ions, i.e., $\alpha_{C\ III} - \alpha_{C\ V} \sim 180^o$. It clearly shows the dependence of the carbon emission on the RMP phase, where the evolutions of C V and C III variation both follow the cosine function, however, in the opposite phases. The cycle length is 360 degrees, in line with the toroidal mode number (n = 1) of the RMP field.

It is found previously in J-TEXT that the three graphite limiters contribute to the carbon source at different levels. Generally, the horizontal limiters offer more carbon impurity than the other two vertical limiters [35]. The high field side limiter is removed in the latest experiments on the J-TEXT tokamak; thus, the LFS limiter is believed to be a main-limiter which provides the most carbon source and has the strongest interaction with edge plasma.

Regarding the opposite phases for C V and C III variation, one possible reason is that the plasma temperature near the O point is higher than that at the X point, leading to a stronger interaction between the LFS limiter and plasma, producing a higher carbon source. But in fact, the impurity screening effect caused by the enhanced outward carbon impurity flux will result in carbon accumulation at the edge region, which can also lead to the stronger C III intensity.

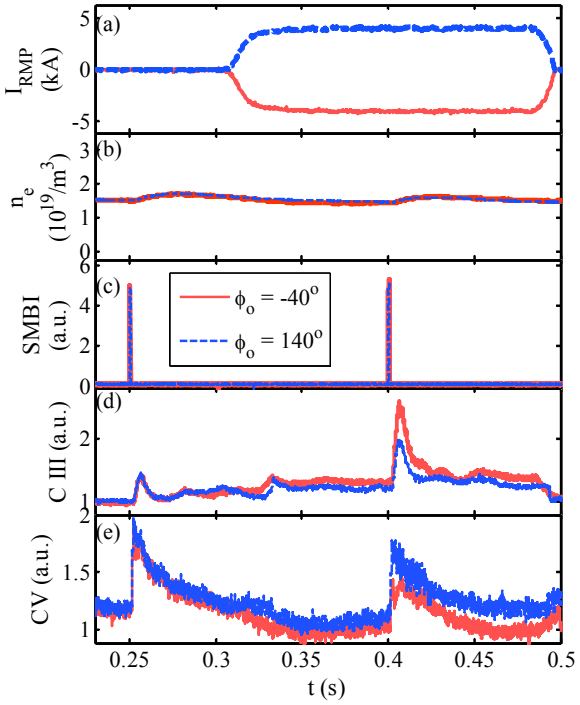

FIG. 7. Evolution of plasma parameters after SMBI injection under RMP at ϕ_o = -40° in shot 1062736 (red) and ϕ_o= 140° in shot 1062760 (blue). (a) RMP current; (b) SMBI signal; (c) Center line-averaged density; (d) C III signal at r= 24 cm; (e) C V signal at r= 20 cm. (I_P = 170kA, B_T = 1.7 T, n_e= 1.5*10^{19}/m^3)

3.3 Impurity transport investigation with active carbon source

To specify the impurity screening effect dependence on the magnetic island phase, we applied the SMBI system to actively inject methane (CH_4), achieving a constant external carbon source pulse. The SMBI injection position is at the bottom of port 10, as shown in FIG. 1. FIG. 7 shows the methane injection results at ϕ_o = -40° with the O point of the magnetic island close to the LFS limiter plate and at ϕ_o = 140° with the X point of the magnetic island close to the LFS limiter plate. It could be seen that the spike of C III caused by the SMBI injection with 3/1 locked magnetic island at 0.4 s, is obviously higher than that without RMP at 0.25 s. For C V, the phenomenon is in the opposite trend, where the height of the C V spike with RMP penetration is lower than 75% of that without RMP. This demonstrates that the 3/1 RMP-induced magnetic island can effectively block the carbon impurity from entrancing the bulk plasma, which is typically described as the impurity screening effect [16, 46]. In line with the previous conclusion, while the O point is closer to the LFS limiter, the impurity screening effect is stronger.

The methane injection by SMBI could induce a transient carbon accumulation in the plasma, showing the rapid formation of the C V signal's spike. In this case, the signal decay time is commonly used to evaluate the impurity confinement [47-49]. The declining period is believed to be dependent on the effective diffusion coefficient as below:

$$D_{eff} \propto a_k \tau_{decay}^{-1} \quad (1)$$

where a_k is the parameter related to the device; τ_{decay} is the impurity decay time which is defined in the exponential expression as

$$P_{rad} \propto \exp\left(-\frac{t}{\tau_{decay}}\right) \quad (2)$$

As shown in FIG. 8(a), the short segments after the peak on the C V signal are chosen to fit the exponential function, and hence to deduce the impurity decay time at the three cases. According to the statistical results of τ_{decay} shown in FIG. 8(b), the impurity decay time shows the dependence on the RMP current. At ϕ_o = -40° case, the decay time drops most after the RMP penetration.

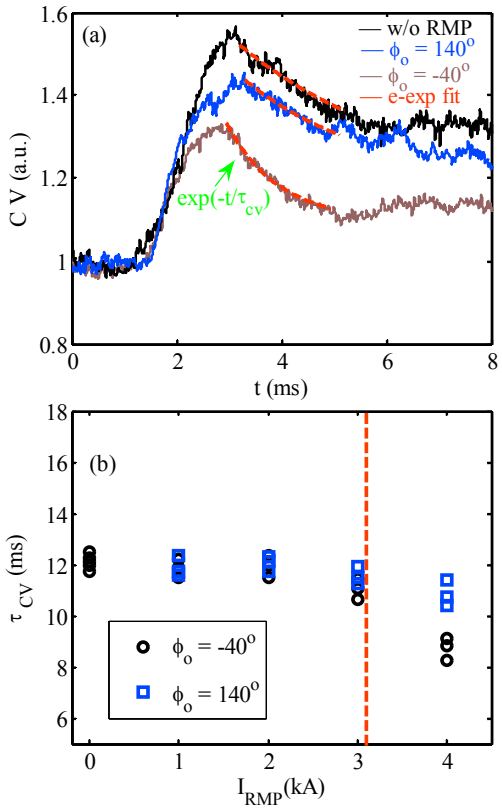

FIG. 8. (a) C V emission evolution after SMBI methane injection. 0s means the injection time. Red dash means the e-exponential fitting. (b) Statistical results of decay time of C V emission and RMP current (blue square: ϕ_o = 140°; black circle: ϕ_o = -40°; Red dash means the threshold of 3/1 penetration.).

IV. Discussion

The SMBI experimental results show the C III spike with RMP penetration is obviously higher than that without RMP, representing the effect of blocking carbon impurity from entrancing the bulk plasma. From the transport's view of point, the convection at the plasma periphery (r > 22cm) is enhanced directed outwards. In the inner region, the impurity decay time drop indicates an enhancement of the impurity diffusion.

For a clearer depiction of the experimental results, the STRAHL code is used to simulate the variation of impurity transport coefficient with the application of RMP in the edge region. STRAHL code is capable of modeling impurity transport in one-dimensional space [35, 50, 51]. It obtains the density distribution of each ionization state and the impurity line emission profile by solving the radial continuity equations. The transport coefficient will be iterated until the

measured emission profile of impurity is reproduced. For a charge stage Z, the coupled radial impurity transport equation can be expressed as

$$\frac{\partial n_z}{\partial t} = \frac{1}{r}\frac{\partial}{\partial r} r\left(D\frac{\partial n_z}{\partial r} - V n_z \right) + Q_z \tag{3}$$

where D is the diffusion coefficient, and V is the convective velocity inside the tokamak plasma (a positive velocity points to the wall). The source or sink term Q is determined by the atomic process of each ionization stage.

During the simulations, the background plasma parameter profiles (including electron temperature, electron density, etc.) are provided as input. The impurity line emission profile measured by diagnostics is also needed for comparison. In the J-TEXT plasma, carbon impurity is the main target to be monitored by impurity line emission diagnostic, and the C III, C V emission profiles can be derived from chord-integral spectral signals with Abel-like inversion [35].

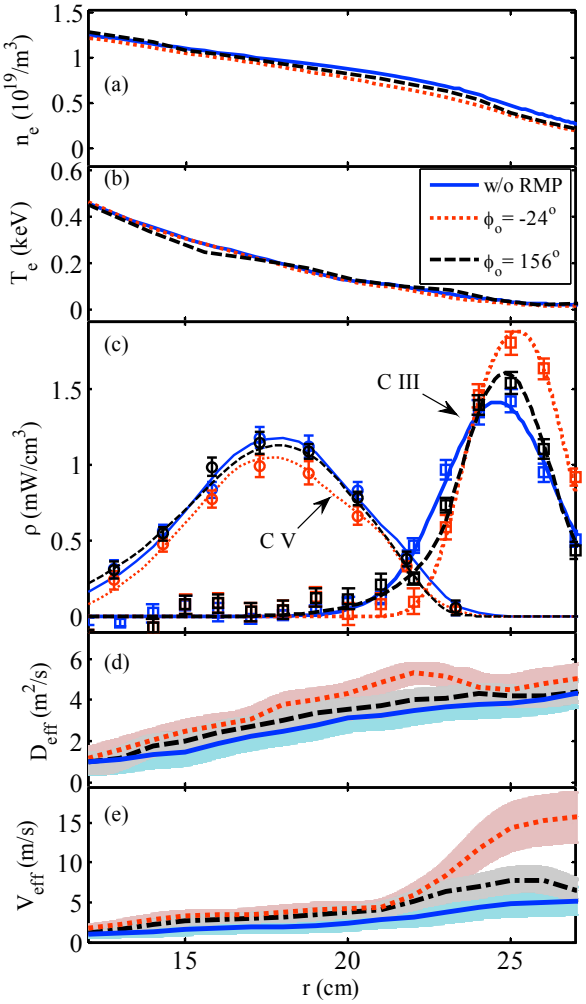

FIG. 9. (a) Density profile; (b) Electron temperature profile; (c) Measured results (point type) and simulated results (line type) of C V and C III emission profile; (d) Carbon impurity effective diffusion coefficient; (e) Carbon impurity effective convection coefficient. The three cases are distinguished by different color: w/o RMP (blue), RMP at ϕ_o = -24° (red), RMP at ϕ_o = 156° (black). The light color represents the error bars of the transport coefficients due to errors in the impurity line emission profiles.

The cases without RMP, and with RMP penetration at ϕ_o = -40° and ϕ_o = 140° are compared, as shown in FIG. 9. The electron density profile in FIG. 9 (a) is provided by POLARIS, and the electronic temperature profile in FIG. 9 (b) is obtained from ECE. The C V and C III emission profiles are composed of two parts: one is the inversion of the impurity line emission signal measured by diagnostics (point type pattern in FIG. 9 (c)); the other is the STRAHL simulation result (line type pattern in FIG. 9 (c)). To be noted that, in this paper the C III emission profile is obtained by averaging the C III from multiple places to fit the one-dimensional code providing a general idea on the RMP role. Thus, the deduced transport coefficients are described as the effective diffusion coefficient and the effective convection coefficient, presented in FIG. 9 (d) and FIG. 9 (e), respectively. Constrained by the C V and C III emission band, the effective region is approximately from r = 12 cm to r = 27 cm. It is obvious that the effective carbon diffusion coefficient in case ϕ_o = -40° is higher than that in case ϕ_o = 140°, which is slightly enhanced compared with the case without RMP. The effective convection velocity at the periphery is much higher with RMP penetration at ϕ_o = -40°, consistent with the conclusion of SMBI experimental results.

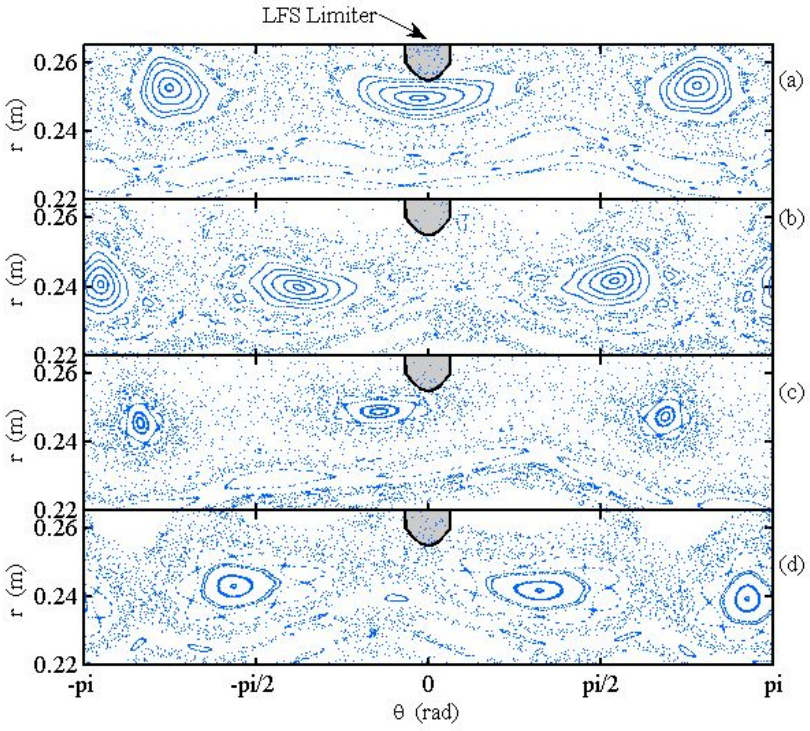

FIG. 10. Poincaré plot of the magnetic fields at limiter position. The poloidal angle of 0 indicates the low-field side, (a) ϕ_o = -24°: (b) ϕ_o = 156°; (c) ϕ_o = -54°; (d) ϕ_o = 126°.

Various studies have reported the transport change with edge magnetic island [19, 13, 14]. One idea is that the enhanced transport is due to the higher radial fraction of the parallel transport with the modified magnetic field topology. The edge magnetic island may also affect the turbulence behavior in the inner region, thus resulting in the difference of impurity transport. Furthermore, it is typically found that the radial electric field is impacted by RMP, due to the unbalanced particle loss [19].

According to the experimental results in J-TEXT, the impurity behavior dependence on the phases of the 3/1 magnetic island is thought to be the result of the interaction between the

magnetic island and the LFS limiter. As shown in FIG. 10, Poincaré plots of the magnetic fields under the four RMP phases (Table 1) are calculated by the nonlinear 3D equilibrium response of the resonant magnetic perturbation field code at the poloidal cross-section in which three limiters are located [52, 53]. The magnetic field lines are partially cut off by the limiter, especially for the case ϕ_o = -24°. This is somewhat similar to the effect of the magnetic island divertor, which is dedicated to achieving a better impurity exhaust [54-57]. For other phases, the magnetic field lines are less cut, leading to the weaker impurity screening effect.

As reported on many devices, in the magnetic island divertor configuration, a large positive electric field with a sharp radial electric field shear is observed, which is considered to be produced by electron loss along the magnetic field line towards the limiter plate [58-60]. In LHD, the radial electric field shear at the boundary is believed to contribute to trigger the formation of an ITB in the electron root plasma. The role of the radial electric field is found to be quite important to prevent the influx of impurities and avoid the radiative collapse. The positive electric field observed in the magnetic island divertor configuration is considered to play an important role for impurity screening [58].

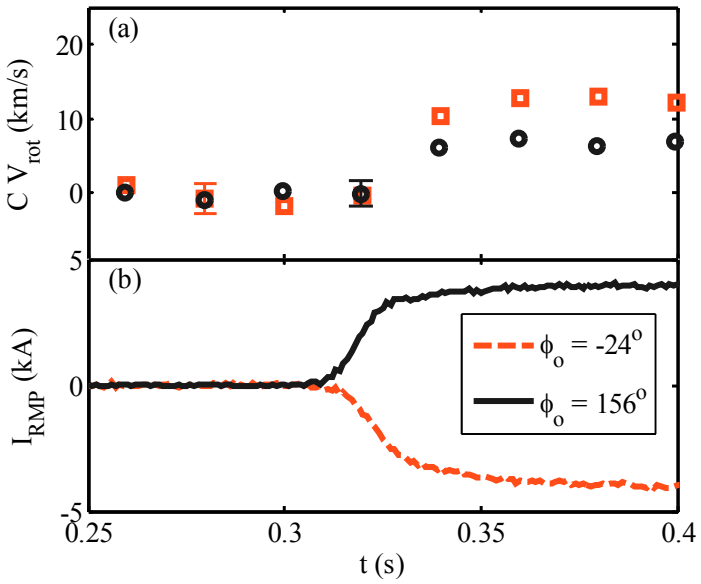

FIG. 11. (a) C V rotation of in the case of RMP at ϕ_o = -24° (red square) and ϕ_o = 156° (black circle). (b) I_{RMP}. (ϕ_o = -24°: red dash; ϕ_o = 156°: black line.)

In the J-TEXT plasma, te change of radial electric field could be indicated by the plasma rotation evolution. As presented in Fig.11, at the case ϕ_o = -24°, the C V rotation increases by ~11 km/s, comparing to ~8 km/s for ϕ_o = 156°. Due to the effect of E×B, the change of the radial electric field will cause the change of the impurity rotation speed. [58, 61]. The modification is in the co-current (I_P) direction, indicating the growth of the outward radial electric field. The electric field may directly enhance the radial particle transport via the classic transport scheme or change the transport through the coupling effect of plasma rotation and turbulence [58, 59].

V. Summary

The 3/1 RMP is applied to generate the edge magnetic island on the J-TEXT. The carbon impurity behavior is found to be affected by the magnetic island, showing the impurity screening effect with C V and C VI intensity decrease and C III intensity increase. The screening role shows

a dependence on the phase of the magnetic island with a stronger impurity screening effect while the O point is approaching the LFS limiter plate. In SMBI methane injection experiments, the C V decay time is reduced with the occurrence of the 3/1 magnetic island, especially for the case with the O point near the LFS limiter plate. Combining the STRAHL simulation, it is concluded that the carbon diffusion is enhanced in the inner region. By comparing the C III signals in the various cases, the edge magnetic island is thought to lead to a high outward convection velocity at edge region. The radial electric field variation due to the interaction of magnetic island and the LFS limiter plate, which can be described as the partial magnetic island divertor configuration, is preliminarily thought to be the key for the impurity transport variation.

The detailed impurity behaviors with the edge magnetic island will be studied with the foreseen introduction of 3-D impurity transport code, such as EMC3. Besides, the synthetic effect of electric field, turbulence and the plasma rotation should be taken into account in the further study, to achieve a deeper understanding of the role the edge magnetic island.

ACKNOWLEDGMENTS

This work was supported by National Key R&D Program of China (2017YFE0301301 & 2017YFE0302000), National Natural Science Foundation of China (No. 11805135 and 11805131) and the Ministry of Science and Technology (Contract No. 2015GB103001). The Shenzhen Clean Energy Research Institute is appreciated. The author's thanks to all the staffs in J-TEXT for their advice and help for analysis of experimental results.

References:

[1]. Doyle, E. J., Houlberg, W. A., Kamada, Y., Mukhovatov, V., et al. Nuclear Fusion. 2007, 47(6): S18.

[2]. Kobayashi, M., Masuzaki, S., Yamada, I., Tamura, N., et al. Physics of Plasmas. 2010, 17(5): 56111.

[3]. Yamada H., Nuclear Fusion. 2011, 51(9): 94021.

[4]. Liang, Y., Koslowski, H. R., Kelly, F. A., Tokar, M. Z., et al. Physical review letters. 2005, 94(10): 105003.

[5]. Schmitz, O., Coenen, J. W., Frerichs, H., Kantor, M., et al. Journal of nuclear materials. 2009, 390: 330-334.

[6]. Petrie, T. W., Evans, T. E., Brooks, N. H., Fenstermacher, M. E., et al. Nuclear Fusion. 2011, 51(7): 73003.

[7]. Lazerson, S. A., Chapman, I. T. Plasma Physics and Controlled Fusion. 2013, 55(8): 84004.

[8]. Hu, Q. M., Nazikian, R., Grierson, B. A., Logan, N. C., et al. Physics of Plasmas. 2019, 26(12): 120702.

[9]. Wang, S. X., Liu, H. Q., Jie, Y. X., Ding, W. X., et al. Nuclear Fusion. 2018, 58(11): 112013.

[10]. Saarelma, S., Alfier, A., Liang, Y., Frassinetti, L., et al. Plasma Physics and Controlled Fusion. 2011, 53(8): 85009.

[11]. Hu, Q., Zhuang, G., Yu, Q., Rao, B., et al. Nuclear Fusion. 2014, 54(6): 64013.

[12]. Hu, Q., Li, J., Wang, N., Yu, Q., et al. Nuclear Fusion. 2016, 56(9): 92009.

[13]. Vogel, G., Zhang, H., Shen, Y., Dai, S., et al. Journal of Plasma Physics. 2021, 87(2).

[14]. Dai, S. Y., Zhang, H. M., Lyu, B., Sun, Y. W., et al. Plasma Physics and Controlled Fusion. 2020, 63(2): 25003.

[15]. Nazikian, R., Paz-Soldan, C., Callen, J. D., DeGrassie, J. S., et al. Physical review letters. 2015, 114(10): 105002.

[16]. Telesca, G., Delabie, E., Schmitz, O., Brezinsek, S., et al. Journal of nuclear materials. 2009, 390: 227-231.

[17]. Zhang, H., Morita, S., Dai, S., Oishi, T., et al. Physics of Plasmas. 2017, 24(2): 22510

[18]. Greiche, A., Liang, Y., Marchuk, O., Bertschinger, G., et al. Plasma physics and controlled fusion. 2008, 51(3): 32001.

[19]. Grierson, B. A., Burrell, K. H., Nazikian, R. M., Solomon, W. M., et al. Physics of Plasmas. 2015, 22(5): 55901.

[20]. Vogel, G., Zhang, H., Shen, Y., Sun, Y., et al. IEEE Transactions on Plasma Science. 2018, 46(5): 1350-1355.

[21]. Tokar, M. Z., Evans, T. E., Gupta, A., Singh, R., et al. Physical review letters. 2007, 98(9): 95001.

[22]. Tokar, M. Z., Evans, T. E., Singh, R., Unterberg, B. Physics of plasmas. 2008, 15(7): 72515.

[23]. Morozov, D. K., Herrera, J., Rantsev Kartinov, V. A. Physics of Plasmas. 1995, 2(5): 1540-1547.

[24]. Tokar, M. Z. Physics of Plasmas. 1999, 6(7): 2808-2815.

[25]. Frerichs, H., Schmitz, O., Evans, T., Feng, Y., et al. Physics of Plasmas. 2015, 22(7): 72508.

[26]. Fenstermacher, M. E., Evans, T. E., Moyer, R. A., Porter, G. D., et al. Journal of nuclear materials. 2007, 363: 476-483.

[27]. Munaretto, S., Chapman, B. E., Holly, D. J., Nornberg, M. D., et al. Plasma Physics and Controlled Fusion. 2015, 57(10): 104004.

[28]. Hinson, E. T., Schmitz, O., Frerichs, H., Abrams, T., et al. Physica Scripta. 2017, 2017(T170): 14048.

[29]. Ge, Z., Yonghua, D., Ming, Z., Kexun, Y., et al. Plasma Science and Technology. 2009, 11(4): 439.

[30]. Zhuang, G., Pan, Y., Hu, X. W., Wang, Z. J., et al. Nuclear Fusion. 2011, 51(9): 94020.

[31]. Liang Y , Wang N , Ding Y H , et al. Nuclear Fusion, 2019.

[32]. Rao, B., Wang, G., Ding, Y. H., Yu, K. X., et al. Fusion engineering and design. 2014, 89(4): 378-384.

[33]. Huang Z, Liang Y, Hu Q, et al. Nuclear Fusion, 2020, 60(6).

[34]. Ding Y, Chen Z, Chen Z, et al. Plasma Science and Technology, 2018.

[35]. Zhang, X. L., Cheng, Z. F., Lin, X. D., Mo, H. S., et al. Fusion Engineering and Design. 2019, 147: 111241.

[36]. Li, Y., Cheng, Z. F., Zhang, X. L., Wang, J. R., et al. Journal of Instrumentation. 2017, 12(06): C6043.

[37]. Mo, H. S., Zhang, X. L., Cheng, Z. F., Zhang, X. Y., et al. Journal of Instrumentation. 2019, 14(10): C10022.

[38]. Chen, J., Zhuang, G., Wang, Z. J., Gao, L., et al. Review of Scientific Instruments. 2012, 83(10): 10E-306E.

[39]. Chen, J., Gao, L., Zhuang, G., Wang, Z. J., et al. Review of Scientific Instruments. 2010, 81(10): 10D-502D.

[40]. Yang, Z. J., Pan, X. M., Ma, X. D., Ruan, B. W., et al. Review of Scientific Instruments. 2016, 87(11): 11E-112E.

[41]. Jin, W., Chen, Z. Y., Huang, D. W., Li, Q. L., et al. Review of Scientific Instruments. 2014, 85(2): 23509.

[42]. Cheng, Z. F., Luo, J., Wang, Z. J., Zhang, Z. P., et al. Review of Scientific Instruments. 2013, 84(7): 73508.

[43]. Cheng, Z. F., Luo, J., Wang, Z. J., Zhang, Z. P., et al. Review of Scientific Instruments. 2014, 85(11): 11E-423E.

[44]. Xiao, J., Yang, Z., Ge, Z., Cheng, Z., et al. IEEE Transactions on Plasma Science. 2013, 41(12): 3675-3679.

[45]. Xiao, J. S., Yang, Z. J., Liu, M. H., Zhuang, G., et al. Journal of Fusion Energy. 2015, 34(5): 1020-1026.

[46]. Corre, Y., Gunn, J., Pegourie, B., Guirlet, R., et al. Nuclear fusion. 2007, 47(2): 119.

[47]. Whyte, D. G., Evans, T. E., Hyatt, A. W., Jernigan, T. C., et al. Physical review letters. 1998, 81(20): 4392.

[48]. Marmar, E. S., Rice, J. E., Terry, J. L., Seguin, F. H. Nuclear Fusion. 1982, 22(12): 1567.

[49]. Mattioli, M., Giannella, R., Myrnas, R., Demichelis, C., et al. Nuclear fusion. 1995, 35(9): 1115.

[50]. Behringer, K., Description of the impurity transport code 'STRAHL', Technical Commission of the European Communities: 1987.

[51]. Dux, R. Impurity transport in tokamak plasmas. 2004.

[52]. Wang Z, Liang Y, Jiang Z, et al. Plasma Science and Technology, 2021.

[53]. Suzuki Y., Plasma Physics and Controlled Fusion, 2017, 59(5): 054008.

[54]. Morisaki T, Masuzaki S, Komori A, et al. Journal of nuclear materials, 2005, 337: 154-160.

[55]. Grigull P, McCormick K, Baldzuhn J, et al. Plasma physics and controlled fusion, 2001, 43(12A): A175.

[56]. Kobayashi M, Feng Y, Morita S, et al. Fusion Science and Technology, 2010, 58(1): 220-231.

[57]. Effenberg F, Brezinsek S, Feng Y, et al. Nuclear Fusion, 2019, 59(10): 106020.

[58]. Ida K, Yoshinuma M, Yokoyama M, et al. Nuclear fusion, 2005, 45(5): 391.

[59]. Krämer-Flecken A, Han X, Windisch T, et al. Plasma physics and controlled fusion, 2019, 61(5): 054003.

[60]. Ido T , Shimizu A , Nishiura M , et al. Plasma Physics and Controlled Fusion, 2010, 52(12):124025.

[61]. Coenen J W , Schmitz O , Unterberg B , et al. Nuclear Fusion, 2011, 51(6):63030-63013.

FIG1

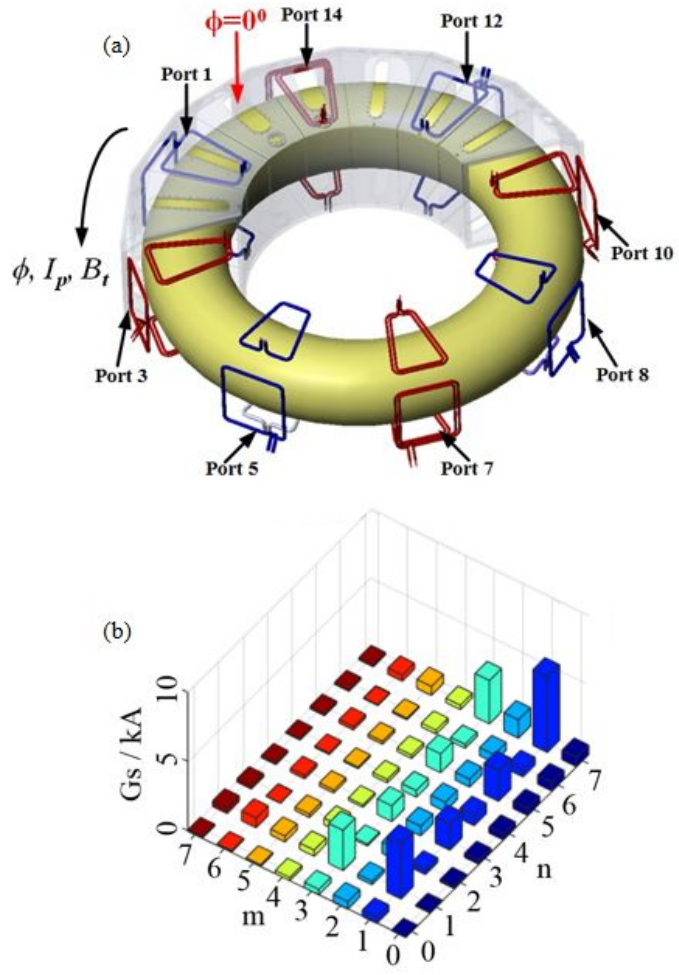
(a)
ϕ=0⁰
Port 14
Port 12
Port 1
Port 10
ϕ, I_p, B_t
Port 3
Port 8
Port 5
Port 7
(b)
Gs / kA
0
5
10
m
n
0
1
2
3
4
5
6
7

FIG2

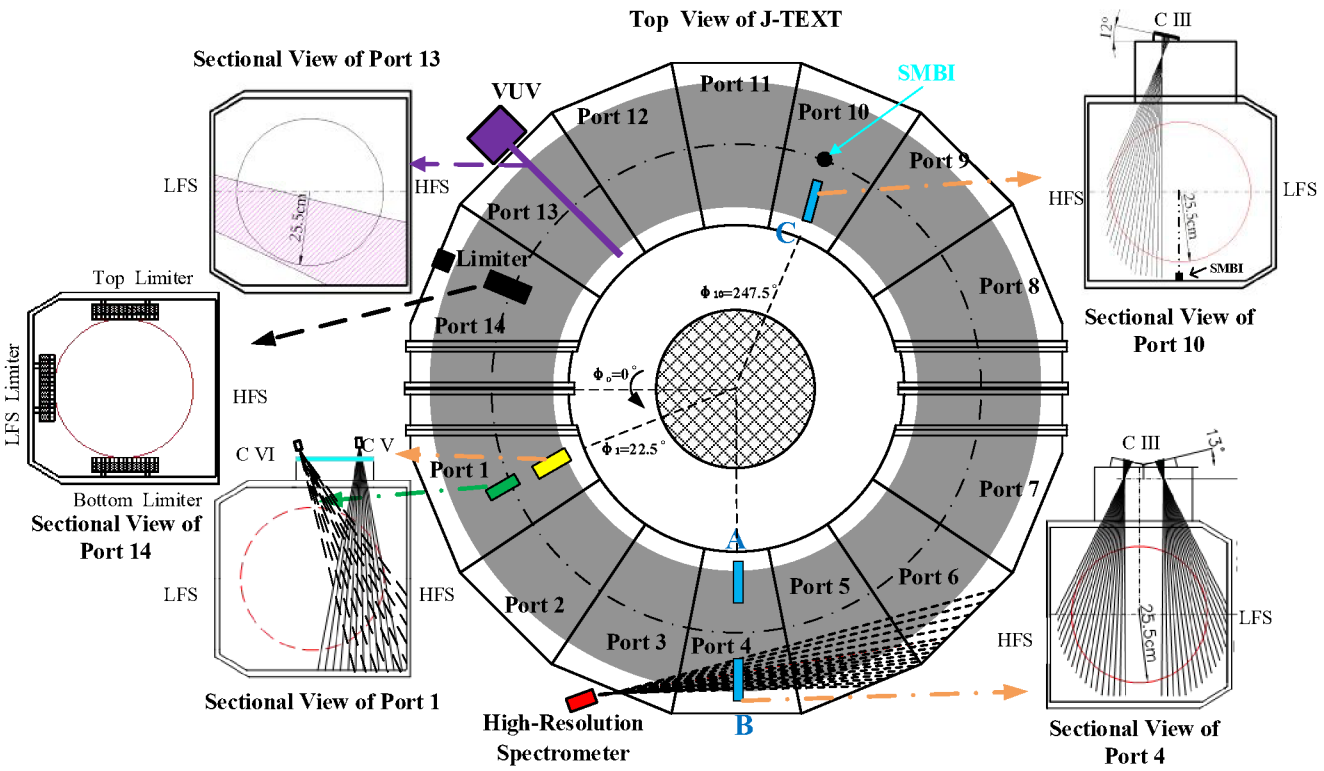
Top View of J-TEXT
Sectional View of Port 13
VUV
SMBI
Port 11
Port 12
Port 10
Port 9
Port 13
Limiter
Port 14
Port 8
Port 1
Port 7
Port 2
Port 5
Port 6
Port 3
Port 4
High-Resolution Spectrometer
LFS
HFS
25.5cm
Top Limiter
LFS Limiter
Bottom Limiter
Sectional View of Port 14
C VI
C V
Sectional View of Port 1
C III
12°
SMBI
Sectional View of Port 10
13°
Sectional View of Port 4
A
B
C

FIG3

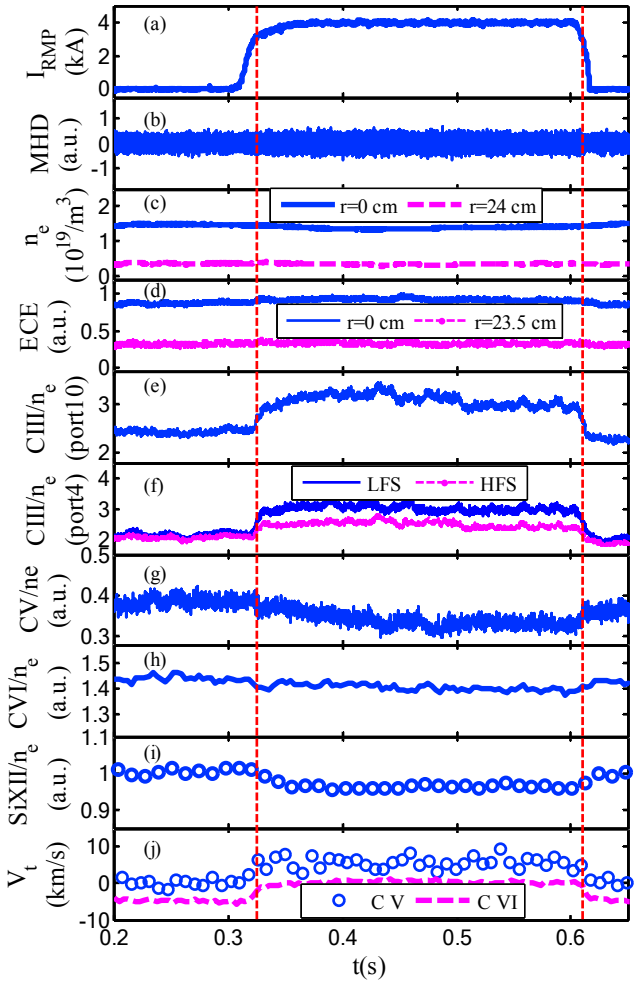
(a)
I_{RMP} (kA)
(b)
MHD (a.u.)
(c)
n_e (10^{19}/m^3)
r=0 cm
r=24 cm
(d)
ECE (a.u.)
r=0 cm
r=23.5 cm
(e)
CIII/n_e (port10)
(f)
CIII/n_e (port4)
LFS
HFS
(g)
CV/ne (a.u.)
(h)
CVI/n_e (a.u.)
(i)
SiXII/n_e (a.u.)
(j)
V_t (km/s)
C V
C VI
t(s)

FIG4

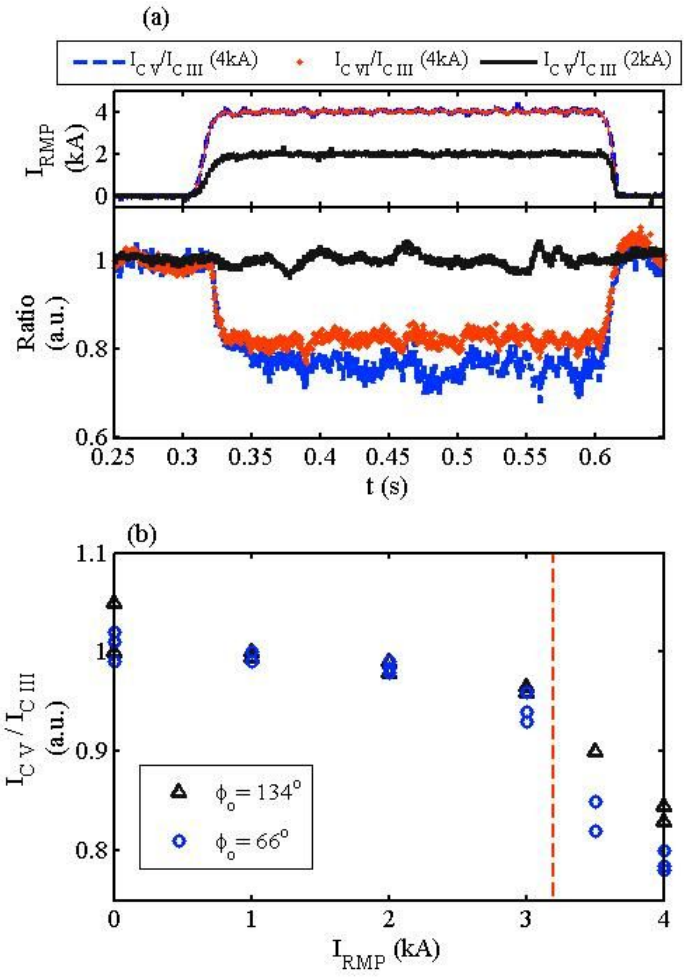
(a)
$I_{C\,V}/I_{C\,III}$ (4kA)
$I_{C\,VI}/I_{C\,III}$ (4kA)
$I_{C\,V}/I_{C\,III}$ (2kA)
I_{RMP} (kA)
Ratio (a.u.)
t (s)
(b)
$I_{C\,V}$ / $I_{C\,III}$ (a.u.)
$\phi_o = 134^o$
$\phi_o = 66^o$
I_{RMP} (kA)

FIG5

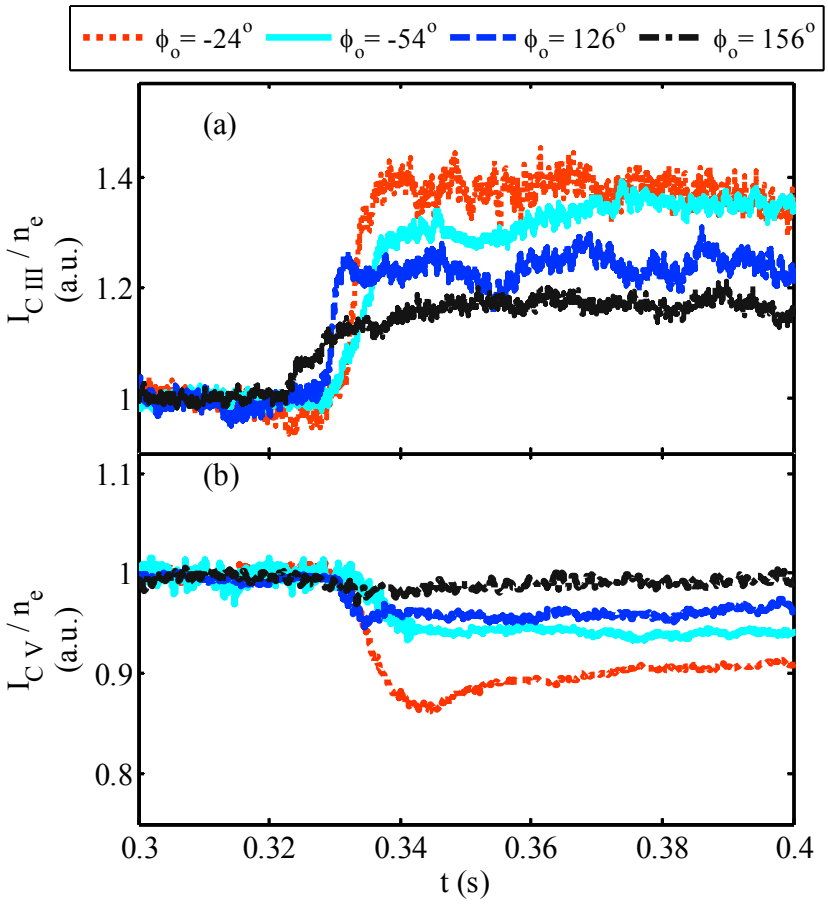
ϕ_o= -24°
ϕ_o= -54°
ϕ_o= 126°
ϕ_o= 156°
(a)
(b)
$I_{C\ III}$ / n_e (a.u.)
$I_{C\ V}$ / n_e (a.u.)
1.4
1.2
1
1.1
1
0.9
0.8
0.3
0.32
0.34
0.36
0.38
0.4
t (s)

FIG6

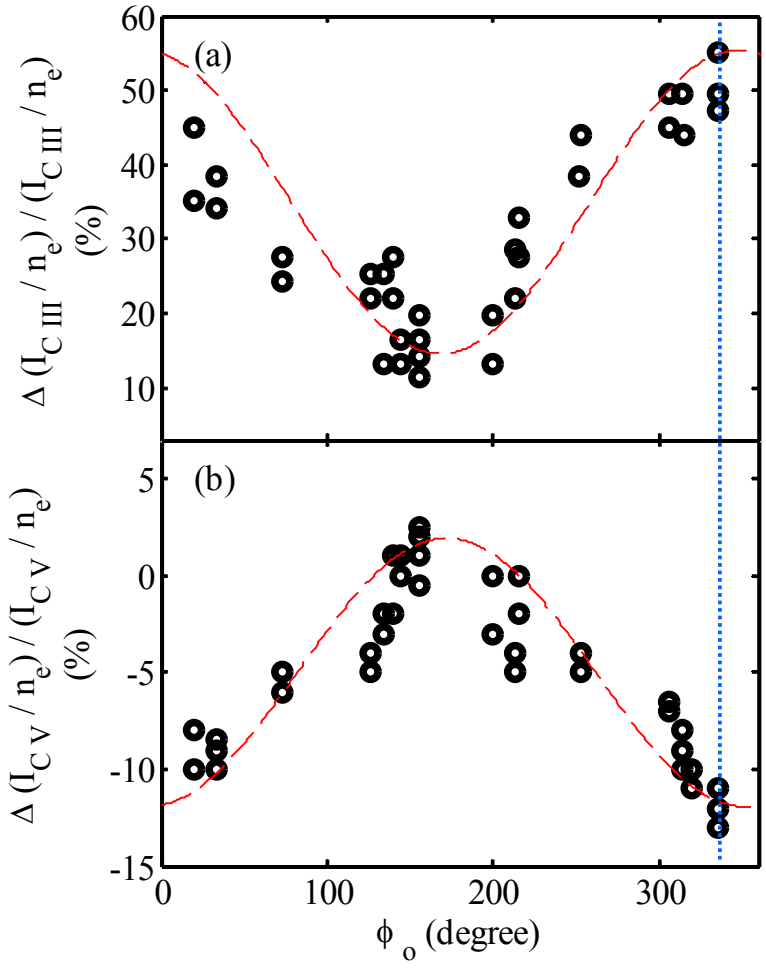
(a)
(b)
Δ (I C III / n e) / (I C III / n e) (%)
Δ (I C V / n e) / (I C V / n e) (%)
ϕ o (degree)
60
50
40
30
20
10
5
0
-5
-10
-15
0
100
200
300

FIG7

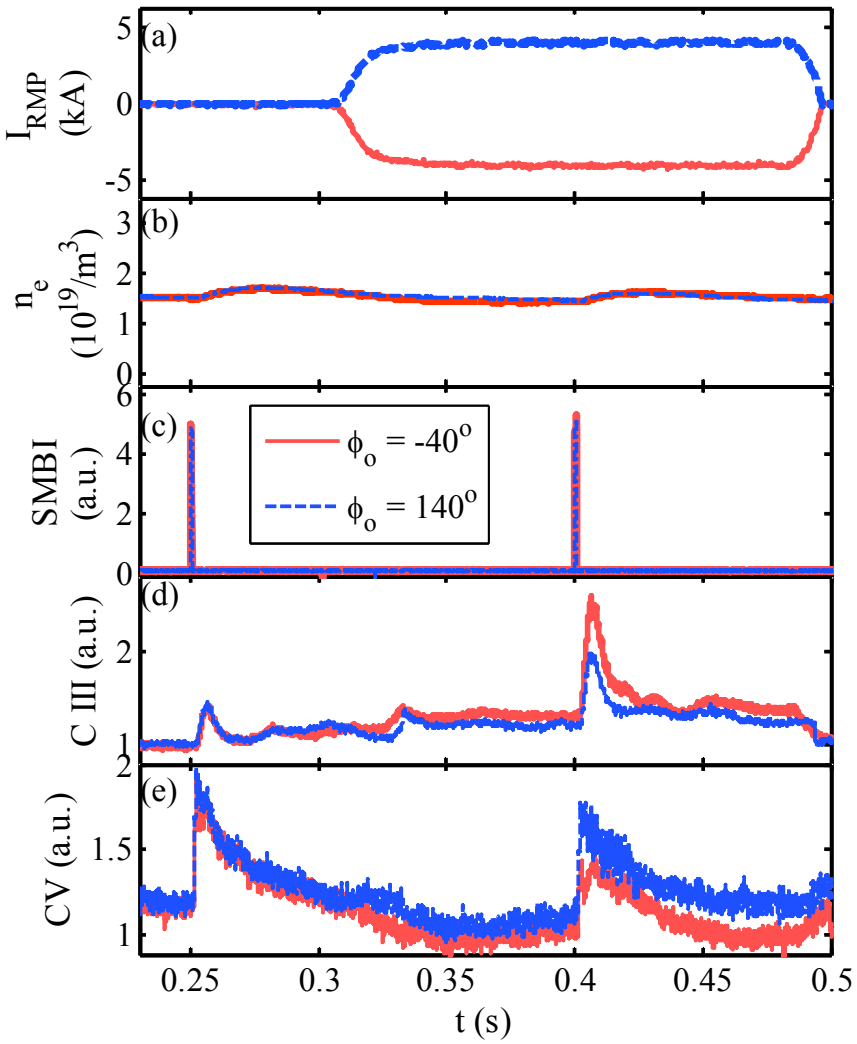
(a)
I_{RMP} (kA)
5
0
-5
(b)
n_e (10^{19}/m^3)
3
2
1
0
(c)
SMBI (a.u.)
6
4
2
0
ϕ_o = -40°
ϕ_o = 140°
(d)
C III (a.u.)
2
1
(e)
CV (a.u.)
2
1.5
1
0.25
0.3
0.35
0.4
0.45
0.5
t (s)

FIG8

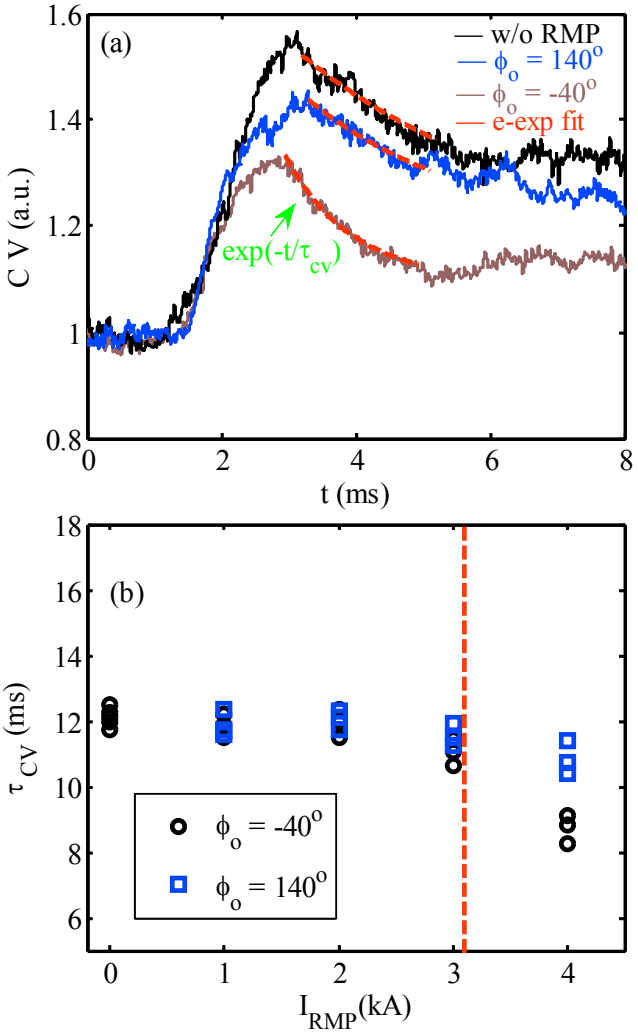
(a)
w/o RMP
ϕ_o = 140°
ϕ_o = -40°
e-exp fit
exp(-t/τ_{cv})
C V (a.u.)
t (ms)
(b)
τ_{CV} (ms)
ϕ_o = -40°
ϕ_o = 140°
I_{RMP}(kA)

FIG9

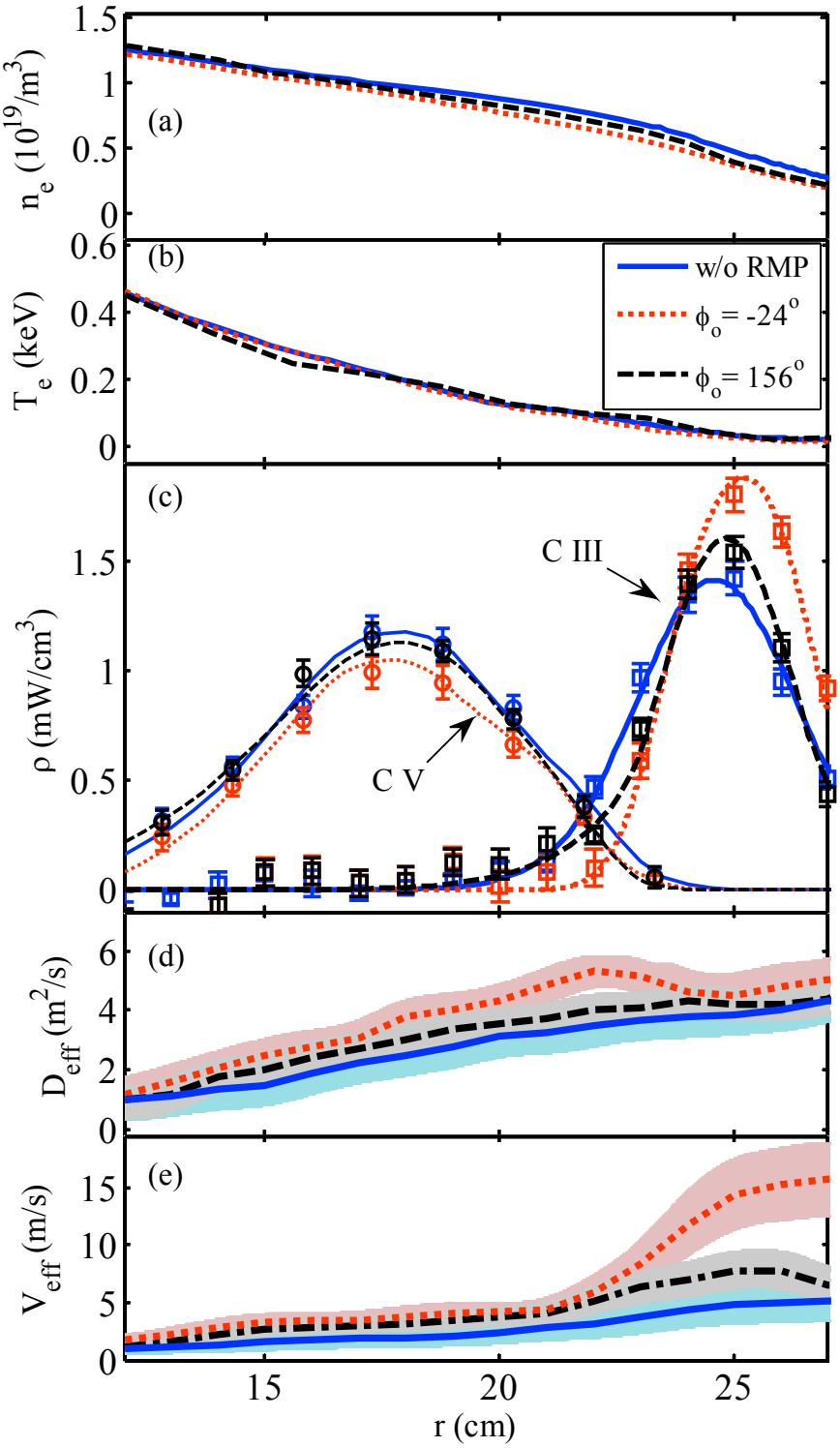
(a)
(b)
(c)
(d)
(e)
w/o RMP
ϕ_o= -24°
ϕ_o= 156°
C III
C V
n_e (10^{19}/m^3)
T_e (keV)
ρ (mW/cm^3)
D_{eff} (m^2/s)
V_{eff} (m/s)
r (cm)

FIG10

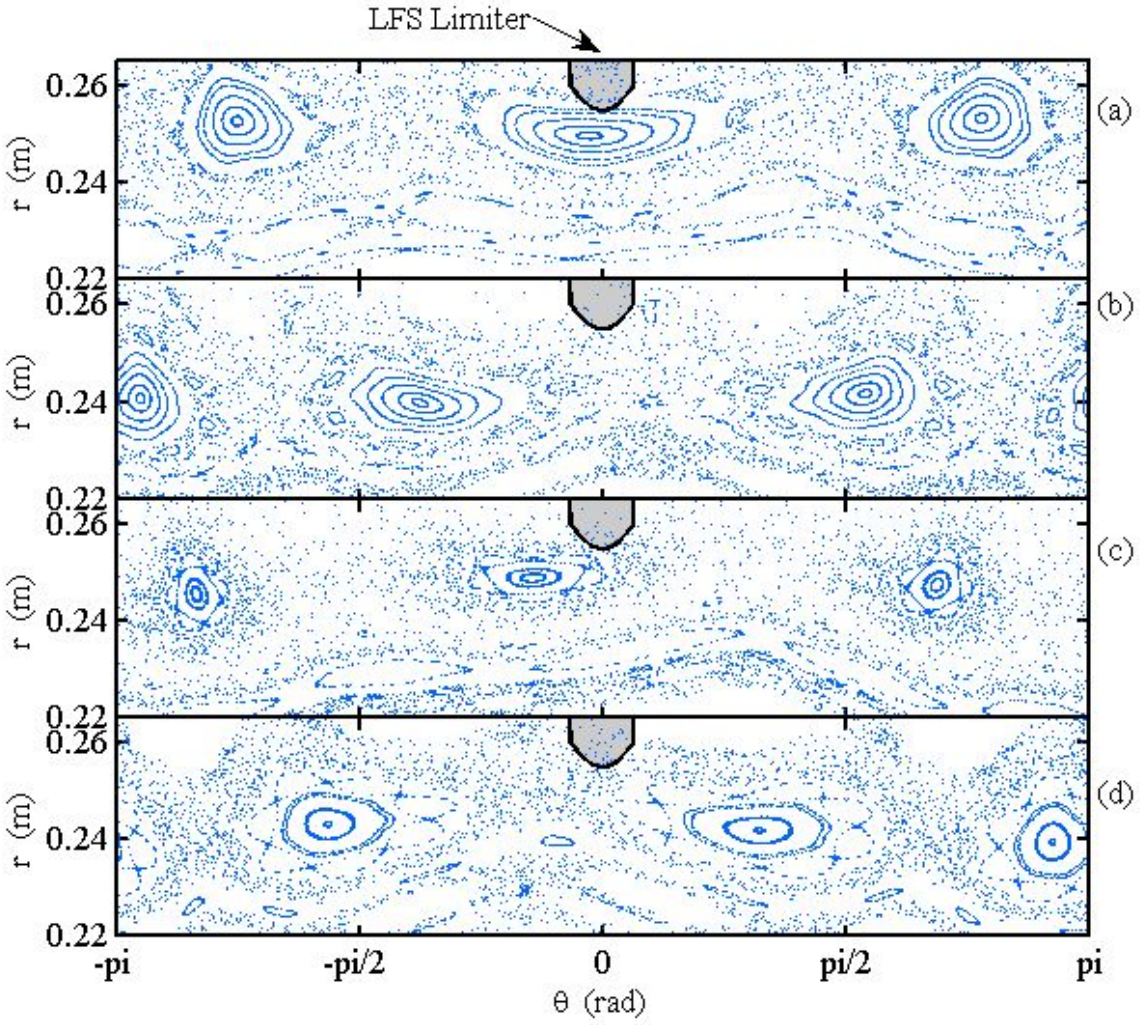

FIG11